Computers and Mathematics with Applications 64 (2012) 798–812

Contents lists available at SciVerse ScienceDirect

Computers and Mathematics with Applications

journal homepage: www.elsevier.com/locate/camwa

Bifurcation and chaos analysis of the porous squeeze film damper mounted gear-bearing system

Cai-Wan Chang-Jian *

Department of Mechanical and Automation Engineering, I-Shou University, 1, Section 1, Hsueh-Cheng Rd., Ta-Hsu Hsiang, Kaohsiung County, Taiwan 840, ROC

ARTICLE INFO

Article history:
Received 8 November 2011
Received in revised form 8 December 2011
Accepted 8 December 2011

Keywords:
Gear
PSFD
Bifurcation
Chaos

ABSTRACT

Porous Squeeze Film Damper (PSFD) has been widely used in the industry and the advantages are very abundant. This study presents a systematic analysis of the dynamic behavior of a gear-bearing system with PSFD under nonlinear suspension, nonlinear oil-film force and nonlinear gear meshing force effect. It can be found that the system exhibits very rich forms of nT-periodic and chaotic vibrations. The bifurcation diagrams also reveal that greater values of permeability may not only improve non-periodic motions effectively, but also suppress dynamic amplitudes of the system. Therefore, we may conclude that PSFD can improve dynamic stability of gear-bearing systems. The results presented in this study provide some useful insights into the design and development of a gear-bearing system for rotating machinery that operates in highly rotational speed and highly nonlinear regimes.

1. Introduction

Many studies have focused on analyzing dynamic behaviors or performance of gears. Ichimaru and Hirano [1] studied the gear mesh model using with constant and found many different dynamic behaviors. Lin et al. [2], Kahraman and Singh [3], Yoon and Rao [4] also studied this kind of spur gear model. Amabili and Fregolent [5] introduced a method based on the measurement of the gear torsional vibrations to identify natural frequency, damping parameters and equivalent gear error of a spur gear pair model. Vedmar and Anersson [6] presented a method to calculate dynamic gear tooth force and bearing forces and the bearing model was under elastic bearing assumption. The simulation results of the elastic model were somewhat different comparing with stiff one. Ozguven and Houser [7,8] performed dynamic analysis on gears with the effects of variable mesh stiffness, damping, gear errors profile modification and backlash. Cai and Hayashi [9] calculated the optimum profile modification to obtain a zero vibration of the gear pair. Umezawa and Sato [10] analyzed a single DOF numerical gear pair model and compared their numerical results with experimental dynamic transmission errors. Mcfadden and Toozhy [11] used the high frequency technique combined with synchronous averaging to detect the failure in rolling element bearings. Litvin et al. [12] proposed a modified geometry of an asymmetric spur gear drive designed as a favorable shape of transmission errors of reduced magnitude and also reduced contact and bending stresses for an asymmetric spur gear drive. Guan et al. [13] performed the finite element method to simulate the geared rotor system constructed from beam and lumped mass/stiffness elements and compared the required actuation effort, control robustness and implementation cost. Giagopulos et al. [14] presented an analysis on the nonlinear dynamics of a gear-pair system supported on rolling element bearings and used a suitable genetic algorithm to measure noise and model error. Theodossiades and Natsiavas [15]

* Tel.: +886 7 6577711x3231; fax: +886 7 6578853.
E-mail address: cwchangjian@mail.isu.edu.tw.

0898-1221/$ – see front matter © 2011 Elsevier Ltd. All rights reserved.
doi:10.1016/j.camwa.2011.12.027

Nomenclature

C_m Damping coefficient of the gear mesh
C_1 Damping coefficients of the supported structure for bearing 1
C_2 Damping coefficients of the supported structure for bearing 2
C_p Damping coefficients of pinion
C_g Damping coefficients of gear
C_{1p} Dimensionless parameter, $C_{1p} = \frac{m_1}{m_p}$
C_{01} Dimensionless parameter, $C_{01} = \frac{K_{p1}}{K_1}$
C_{2p} Dimensionless parameter, $C_{2p} = \frac{m_2}{m_p}$
C_{02} Dimensionless parameter, $C_{02} = \frac{K_{p1}}{K_2}$
E_p Eccentricity ratio of pinion, e_p/d
E_g Eccentricity ratio of gear, e_g/d
e_p Eccentricity of pinion
e_g Eccentricity of gear
F_{x1} Oil film force in the horizontal direction for bearing 1
F_{y1} Oil film force in the vertical direction for bearing 1
F_{x2} Oil film force in the horizontal direction for bearing 2
F_{y2} Oil film force in the vertical direction for bearing 2
f_{e1} and $f_{\varphi 1}$ Viscous damping forces in the radial and tangential directions for the center of journal 1
f_{e2} and $f_{\varphi 2}$ Viscous damping forces in the radial and tangential directions for the center of journal 2
f Dimensionless parameter, $f = \frac{m_p g}{dK_{p1}}$
f_g Dimensionless parameter, $f_g = \frac{K_{p1} g}{dm_p}$
f_e, f_φ Components of the fluid film force in radial and tangential directions
G_{py}, G_{gy} Inertia forces in the vertical gear mesh direction for pinion and gear,

$$G_{py} = m_p e_p \ddot{\theta}_1 \cos\theta_1, \qquad G_{gy} = m_g e_g \ddot{\theta}_2 \cos\theta_2$$

K_m Stiffness coefficient of the gear mesh
K_{11}, K_{12} Stiffness coefficients of the springs supporting the two bearing housings for bearing 1
K_{21}, K_{22} Stiffness coefficients of the springs supporting the two bearing housings for bearing 2
K_{p1} Stiffness coefficients of pinion
K_{p2} Stiffness coefficients of gear
L Bearing length
L_{py}, L_{gy} Centrifugal forces in the vertical gear mesh direction for pinion and gear,

$$L_{py} = m_p e_p \omega_p^2 \sin\theta_1, \qquad L_{gy} = m_g e_g \omega_g^2 \sin\theta_2$$

m_1 Mass of the bearing housing for bearing 1
m_2 Mass of the bearing housing for bearing 2
m_p Mass of the pinion
m_g Mass of the gear
O_1 Geometric centers of the bearing 1
O_2 Geometric centers of the bearing 2
O_{j1} Geometric centers of the journal 1
O_{j2} Geometric centers of the journal 2
O_g Center of gravity of the gear
O_p Center of gravity of the pinion
p Pressure distribution in the fluid film
R Inner radius of the bearing housing
r Radius of the journal.
s Rotational speed ratio, $s = (\frac{\Omega^2}{\omega_n^2})^{1/2}$
s_1 Dimensionless parameter, $s_1^2 = C_{o1} C_{1p} s^2$
s_2 Dimensionless parameter, $s_2^2 = C_{o2} C_{2p} s^2$
W_{cx} Dynamic gear mesh force in the horizontal direction,

$$W_{cx} = C_m(\dot{X}_p - \dot{X}_g - e_p \Omega \sin(\Omega t)) + K_m(X_p - X_g - e_p \cos(\Omega t))$$

W_{cy} Dynamic gear mesh force in the vertical direction,

$$W_{cy} = C_m(\dot{Y}_p - \dot{Y}_g - e_p\Omega\cos(\Omega t)) + K_m(Y_p - Y_g - e_p\sin(\Omega t))$$

X_j, Y_j Horizontal and vertical coordinates, $j = 1, 2, j1, j2, p, g$
X_{p0}, Y_{p0}, X_{g0}, Y_{g0} Damper static displacements
x_j, y_j X_j/c, Y_j/c, $j = 1, 2, j1, j2, p, g$
α Pressure angle
α_1 Dimensionless parameter, $\alpha_1 = \frac{K_{12}d^2K_{p1}}{m_1m_p}$
α_2 Dimensionless parameter, $\alpha_2 = \frac{K_{22}d^2K_{p1}}{m_2m_p}$
β Dimensionless parameter, $\beta = E_p/16$
β_g Dimensionless parameter, $\beta_g = E_p/16$
ξ_1 Dimensionless parameter, $\xi_1 = \frac{C_1}{2\sqrt{K_1m_1}}$
ξ_2 Dimensionless parameter, $\xi_2 = \frac{C_p}{2\sqrt{K_{p1}m_p}}$
ξ_3 Dimensionless parameter, $\xi_3 = \frac{C_m}{2\sqrt{K_{p1}m_p}}$
ξ_4 Dimensionless parameter, $\xi_4 = \frac{C_g}{2\sqrt{\frac{K_{p1}}{m_p}m_g}}$
ξ_5 Dimensionless parameter, $\xi_5 = \frac{C_m\sqrt{m_p}}{2m_g\sqrt{K_{p1}}}$
ξ_6 Dimensionless parameter, $\xi_6 = \frac{C_2}{2\sqrt{K_2m_2}}$
Λ Dimensionless parameter, $\Lambda = \frac{K_m}{K_{p1}}$
Λ_g Dimensionless parameter, $\Lambda_g = \frac{K_mm_p^2}{m_gK_{p1}^2}$
ρ Mass eccentricity of the rotor
ϕ Rotational angle, $\phi = \omega t$
φ_i Attitude angle of the line O_iO_{ji} from the X_i-coordinate (see Fig. 1)
Ω Rotational speed of the shaft
ω_n Natural frequency, $\omega_n = \sqrt{K_{p1}/m_p}$
ω_g Angular velocity of gear, $\omega_g = \Omega/8$
ω_p Angular velocity of pinion, $\omega_p = \Omega/4$
θ_1 Angular displacement of pinion, $\theta_1 = \omega_p t$
θ_2 Angular displacement of gear, $\theta_2 = \omega_g t$
μ Oil dynamic viscosity
ε_1 Eccentricity ratio, $\varepsilon_1 = e_1/d$
ε_2 Eccentricity ratio, $\varepsilon_2 = e_2/d$
ψ Dimensionless permeability, $\psi = \frac{12\Phi H}{c^3}$

investigated dynamic responses and stability characteristics of rotordynamic systems interconnected with gear pairs and supported on oil journal bearings. They found many non-periodic dynamic behaviors. They [16] also analyzed the motor-driven gear-pair systems with backlash and found periodic and chaotic dynamics in this system. Chang-Jian and Chen [17,18] studied bifurcation analysis and chaotic analysis of a flexible rotor supported by turbulent journal bearings and couple-stress fluid film bearings with nonlinear suspension. They found a lot of non-periodic motions, i.e. quasi-periodic motions, subharmonic motions and the so-called chaotic motions happening in those rotor-bearing systems. They also prove the couple-stress fluid can improve dynamic stability and emphasize the importance of turbulent flow effect considering in highly rotational turbo-machineries. Wang and Chen [19,20] studied nonlinear dynamic and bifurcation analysis of externally pressurized porous gas journal bearings and found very rich forms of nT-periodic and chaotic vibrations. Meanwhile, Wang et al. [21,22] applied the so-called differential transform method to analyze bifurcation and chaotic dynamic behaviors of an AFM probe tip. They found some wonderful and interesting nonlinear phenomena. Chang-Jian and Yau [23] studied nonlinear dynamics of the rotor-bearing system equipped with hybrid squeeze film damper and lubricated with couple stress fluid and also the dynamics of systems with hydraulic control. Liu et al. [24] proposed the designing and experimental verification of a novel hydrodynamic grooved journal bearing.

Although virtually all physical phenomena in the real world can be regarded as nonlinear, most of these phenomena can be simplified to a linear form given a sufficiently precise linearization technique. However, this simplification is inappropriate for high-power, high rotational speed gear systems, and its application during the design and analysis stage

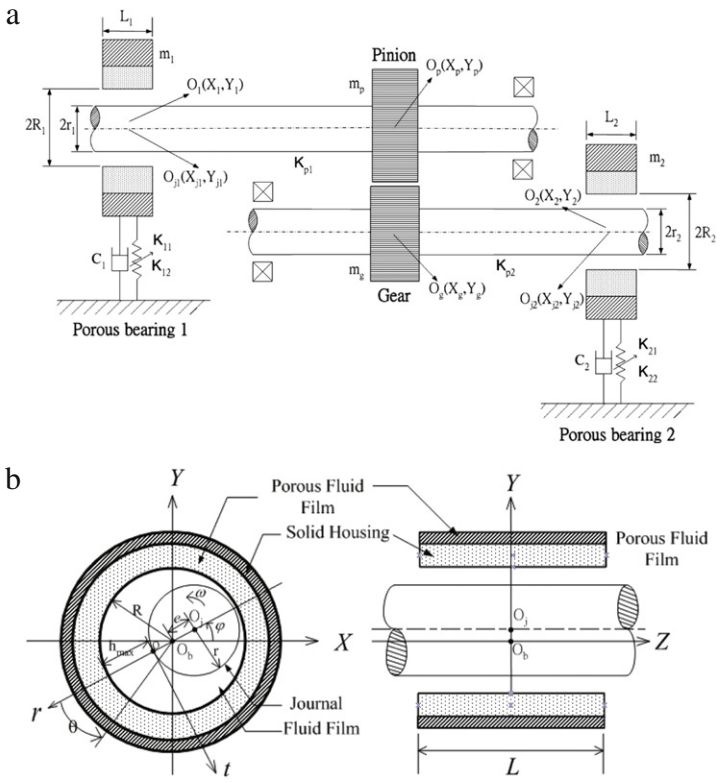

Fig. 1. Schematic illustration of the gear-bearing system with PSFD and cross section of the porous film.

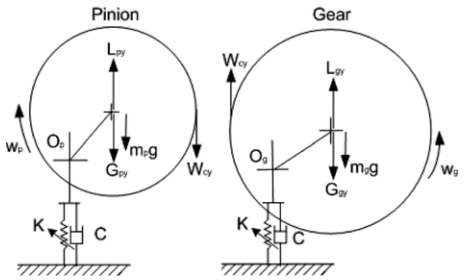

Fig. 2. Model of force diagram for pinion and gear.

may result in a flawed or potentially dangerous operation. As a result, nonlinear analysis methods are generally preferred within engineering and academic circles. The current study performs a nonlinear analysis of the dynamic behavior of a gear pair system equipped with short journal bearings under strongly nonlinear gear meshing force effect and nonlinear suspension effect. The non-dimensional equation of the gear-bearing system is then solved using the Runge–Kutta method. The non-periodic behavior of this system is characterized using phase diagrams, power spectra, Poincaré maps, bifurcation diagrams, Lyapunov exponents and the fractal dimension of the system.

2. Mathematical model

The model discussed in this study is the porous squeeze film damper mounted on a gear-bearing system with assumptions of nonlinear suspension (hard spring effect), short journal bearing, strongly nonlinear gear meshing force and strongly nonlinear fluid film force effect as shown in Fig. 1(a). Fig. 1(b) presents the cross section of the porous film. Fig. 2 presents a schematic illustration of the dynamic model considered between gear and pinion. $O_g(X_g, Y_g)$ and $O_p(X_p, Y_p)$ are the gravity centers of the gear and pinion, respectively. $O_1(X_1, Y_1)$ and $O_2(X_2, Y_2)$ are the geometric centers of the bearing 1 and bearing 2, respectively. $O_{j1}(X_{j1}, Y_{j1})$ and $O_{j2}(X_{j2}, Y_{j2})$ are the geometric centers of the journal 1 and journal 2, respectively. m_1 is the mass of the bearing housing for bearing 1 and m_2 is the mass of the bearing housing for bearing 2. m_p is the mass of the pinion and m_g is the mass of the gear. K_{p1} and K_{p2} are the stiffness coefficients of the shafts. K_{11}, K_{12}, K_{21} and K_{22} are

the stiffness coefficients of the springs supporting the two bearing housings for bearing 1 and bearing 2. C_1 and C_2 are the damping coefficients of the supported structure for bearing 1 and bearing 2, respectively. K is the stiffness coefficient of the gear mesh. C is the damping coefficient of the gear mesh, e is the static transmission error and varies as a function of time. Note that (X_i, Y_i) are fixed coordinates, while (e_i, φ_i) are rotational coordinates, in which e_i is the offset of the journal center and φ_i is the attitude angle of the rotor relative to the X-coordinate direction.

2.1. Principles of force equilibrium

According to the principles of force equilibrium, the forces acting at the center of journal 1, i.e. $O_{j1}(X_{j1}, Y_{j1})$ and center of journal 2, i.e. $O_{j2}(X_{j2}, Y_{j2})$ are given by

$$F_{x1} = f_{e1}\cos\varphi_1 + f_{\varphi 1}\sin\varphi_1 = K(X_p - X_{j1})/2, \tag{1}$$

$$F_{y1} = f_{e1}\sin\varphi_1 - f_{\varphi 1}\cos\varphi_1 = K(Y_p - Y_{j1})/2, \tag{2}$$

$$F_{x2} = f_{e2}\cos\varphi_2 + f_{\varphi 2}\sin\varphi_2 = K(X_g - X_{j2})/2, \tag{3}$$

$$F_{y2} = f_{e2}\sin\varphi_2 - f_{\varphi 2}\cos\varphi_2 = K(Y_g - Y_{j2})/2, \tag{4}$$

in which f_{e1} and $f_{\varphi 1}$ are the viscous damping forces in the radial and tangential directions for the center of journal 1, respectively, and f_{e2} and $f_{\varphi 2}$ are the viscous damping forces in the radial and tangential directions for the center of journal 2, respectively.

2.2. Nonlinear fluid film force

In this study, the modified Reynolds equation and the short bearing assumption ($\frac{L}{D} < 0.25$, $\frac{\partial p}{\partial \theta} \ll \frac{\partial p}{\partial z}$) is used.

$$\frac{\partial}{\partial z}\left(12\Phi H\frac{\partial p}{\partial z}\right) = 6\mu U\frac{\partial h}{\partial x} + 12\mu\frac{\partial h}{\partial t} \tag{5}$$

where Φ is permeability of porous ring, Φ can also be performed as $\Phi = \frac{Q_\mu H}{\Delta p A}$, A is area of porous ring, H is film thickness of porous ring, Δp is pressure difference of porous ring, $\frac{\partial h}{\partial x} = -\frac{c\varepsilon}{R}\sin\theta$, $\frac{\partial h}{\partial t} = c\dot{\varepsilon}\cos\theta + c\varepsilon\dot{\varphi}\sin\theta$, $x = R\theta$, $U = R\omega$, $\varepsilon = \frac{e}{c}$ and $h = c(1 + \varepsilon\cos(\gamma - \varphi(t))) = c(1 + \varepsilon\cos\theta)$. Then Reynolds equation can be rewritten as

$$\frac{\partial^2 p}{\partial z^2} = \frac{-6\mu\omega c\varepsilon\sin\theta + 12\mu(c\dot{\varepsilon}\cos\theta + c\varepsilon\dot{\varphi}\sin\theta)}{12\Phi H} \tag{6}$$

with boundary conditions $\begin{cases} \frac{\partial p}{\partial z} = 0, & z = 0 \\ p = 0, & z = \pm\frac{L}{2} \end{cases}$

$$\text{then } p = -\frac{3\mu c}{12\Phi H}[(\omega - 2\dot{\varphi})\varepsilon\sin\theta - 2\dot{\varepsilon}\cos\theta]\left(z^2 - \frac{L^2}{4}\right). \tag{7}$$

The resulting damping forces about the journal center in the radial and tangential directions are determined by integrating equation (7) over the area of the journal sleeve on the basis of the hypothesis of cavitating conditions with π-film.

$$f_r = \int_0^\pi \int_{-\frac{L}{2}}^{\frac{L}{2}} p(\theta, z)R\cos\theta dz d\theta \tag{8}$$

$$f_t = \int_0^\pi \int_{-\frac{L}{2}}^{\frac{L}{2}} p(\theta, z)R\sin\theta dz d\theta. \tag{9}$$

Let $\psi = \frac{12\Phi H}{c^3}$, $f_e = -f_r$, $f_\varphi = -f_t$

$$f_e = -\frac{\mu L^3 R}{2c^2\psi}\int_0^\pi \{[(\omega - 2\dot{\varphi})\varepsilon\sin\theta - 2\dot{\varepsilon}\cos\theta]\sin\theta\}\, d\theta \tag{10}$$

$$f_\varphi = -\frac{\mu L^3 R}{2c^2\psi}\int_0^\pi \{[(\omega - 2\dot{\varphi})\varepsilon\sin\theta - 2\dot{\varepsilon}\cos\theta]\sin\theta\}\, d\theta. \tag{11}$$

Substituting Eqs. (10) and (11) into Eqs. (1)–(4), respectively, enables the values of F_{x1}, F_{x2}, F_{y1} and F_{y2} to be obtained.

2.3. Equations of motion

The differential equations of motion used to describe geometric centers of gear and pinion ($O_g(X_g, Y_g)$ and $O_p(X_p, Y_p)$) can be written as

$$m_p\ddot{X}_p + C\dot{X}_p + KX_p = W_{cx} + F_{x1} + KX_{p0} \tag{12}$$

$$m_p\ddot{Y}_p + C\dot{Y}_p + KY_p = L_{py} - G_{py} - W_{cy} - m_pg + F_{y1} + KY_{p0} \tag{13}$$

$$m_g\ddot{X}_g + C\dot{X}_g + KX_g = -W_{cx} + F_{x2} + KX_{g0}, \tag{14}$$

$$m_g\ddot{Y}_g + C\dot{Y}_g + KY_g = L_{py} - G_{py} + W_{cy} - m_gg + F_{y2} + KY_{g0}, \tag{15}$$

where L_{py} and L_{gy} are the centrifugal forces in the vertical gear mesh direction for pinion and gear, G_{py} and G_{gy} are the inertia forces in the vertical gear mesh direction for pinion and gear, W_{cx} is the dynamic gear mesh force in the horizontal direction, and W_{cy} is the dynamic gear mesh force in the vertical direction. L_{py}, L_{gy}, G_{py}, G_{gy}, W_{cx} and W_{cy} can be performed as

$$L_{py} = m_pe_p\omega_p^2 \sin\theta_1, \tag{16}$$

$$L_{gy} = m_ge_g\omega_g^2 \sin\theta_2, \tag{17}$$

$$G_{py} = m_pe_p\ddot{\theta}_1 \cos\theta_1, \tag{18}$$

$$G_{gy} = m_ge_g\ddot{\theta}_2 \cos\theta_2, \tag{19}$$

$$W_{cx} = C_m(\dot{X}_p - \dot{X}_g - e_p\Omega \sin(\Omega t)) + K_m(X_p - X_g - e_p \cos(\Omega t)), \tag{20}$$

$$W_{cy} = C_m(\dot{Y}_p - \dot{Y}_g - e_p\Omega \cos(\Omega t)) + K_m(Y_p - Y_g - e_p \sin(\Omega t)). \tag{21}$$

Substituting Eqs. (16)–(21) into Eqs. (12)–(15), yields the following equations.

$$m_p\ddot{X}_p + C\dot{X}_p + KX_p = C_m(\dot{X}_p - \dot{X}_g - e_p\Omega \sin(\Omega t)) + K_m(X_p - X_g - e_p \cos(\Omega t)) + F_{x1} + KX_{p0}, \tag{22}$$

$$\begin{aligned} m_p\ddot{Y}_p + C\dot{Y}_p + KY_p \;=\; & m_pe_p\omega_p^2 \sin\theta_1 - C_m(\dot{Y}_p - \dot{Y}_g - e_p\Omega \cos(\Omega t)) \\ & - K_m(Y_p - Y_g - e_p \sin(\Omega t)) - m_pg + F_{y1} + KY_{p0}, \end{aligned} \tag{23}$$

$$m_g\ddot{X}_g + C\dot{X}_g + KX_g = -C_m(\dot{X}_p - \dot{X}_g - e_p\Omega \sin(\Omega t)) - K_m(X_p - X_g - e_p \cos(\Omega t)) + F_{x2} + KX_{g0}, \tag{24}$$

$$\begin{aligned} m_g\ddot{Y}_g + C\dot{Y}_g + KY_g \;=\; & m_ge_g\omega_g^2 \sin\theta_2 - C_m(\dot{Y}_p - \dot{Y}_g - e_p\Omega \cos(\Omega t)) \\ & + K_m(Y_p - Y_g - e_p \sin(\Omega t)) - m_gg + F_{y2} + KY_{g0}. \end{aligned} \tag{25}$$

The equations of motion of the center of bearing 1 (X_1, Y_1) and the center of bearing 2 (X_2, Y_2) under the assumption of nonlinear suspension can be written as

$$m_1\ddot{X}_1 + c_1\dot{X}_1 + k_{11}X_1 + k_{12}X_1^3 = F_{x1}, \tag{26}$$

$$m_1\ddot{Y}_1 + c_1\ddot{Y}_1 + k_{11}Y_1 + k_{12}Y_1^3 = -m_1g + F_{y1}, \tag{27}$$

$$m_2\ddot{X}_2 + c_2\dot{X}_2 + k_{21}X_2 + k_{22}X_2^3 = F_{x2}, \tag{28}$$

$$m_2\ddot{Y}_2 + c_2\ddot{Y}_2 + k_{21}Y_2 + k_{22}Y_2^3 = -m_2g + F_{y2}. \tag{29}$$

2.4. Dimensionless dynamic equations of motion

Introducing the following non-dimensional parameters:

$$x_j = X_j/d, \quad y_j = Y_j/d, \quad j = 1, 2, j1, j2, p, g, \quad \frac{d}{dt} = \Omega\frac{d}{d\phi}, \quad s^2 = \frac{\Omega^2}{\omega_n^2}, \quad \omega_n^2 = K/m_p,$$

$$\omega_g = \Omega/8, \quad \omega_p = \Omega/4, \quad \beta = E_p/16, \quad \beta_g = E_p/16, \quad f = \frac{m_pg}{dK}, \quad f_g = \frac{Kg}{dm_p},$$

$$\xi_1 = \frac{C_1}{2\sqrt{K_1m_1}}, \quad \xi_2 = \frac{C}{2\sqrt{Km_p}}, \quad \xi_3 = \frac{C_m}{2\sqrt{Km_p}}, \quad \xi_4 = \frac{C}{2\sqrt{\frac{K}{m_p}}m_g}, \quad \xi_5 = \frac{C_m\sqrt{m_p}}{2m_g\sqrt{K}},$$

$$\xi_6 = \frac{C_2}{2\sqrt{K_2m_2}}, \quad C_{1p} = \frac{m_1}{m_p}, \quad C_{01} = \frac{K}{k_1}, \quad s_1^2 = C_{o1}C_{1p}s^2, \quad C_{2p} = \frac{m_2}{m_p},$$

$$C_{02} = \frac{K}{k_2}, \quad s_2^2 = C_{o2}C_{2p}s^2, \quad \Lambda = \frac{K_m}{K}, \quad \Lambda_g = \frac{K_mm_p^2}{m_gK^2}, \quad \alpha_1 = \frac{K_{12}d^2K}{m_1m_p}, \quad \alpha_1 = \frac{K_{22}d^2K}{m_2m_p}.$$

Eqs. (1)–(4) and (22)–(29) can be expressed as

$$\begin{aligned}\varepsilon_1' &= \frac{\beta_1 cK_p[(y_p - y_1 - \varepsilon_1\sin\varphi_1)\cos\varphi_1 - (x_p - x_1 - \varepsilon_1\cos\varphi_1)\sin\varphi_1]}{4\alpha_1(\gamma_1\delta_1 - \beta_1^2)\omega} \\ &\quad - \frac{\delta_1 cK_p[(x_p - x_1 - \varepsilon_1\cos\varphi_1)\cos\varphi_1 + (y_2 - y_1 - \varepsilon_1\sin\varphi_1)\sin\varphi_1]}{4\alpha_1(\gamma_1\delta_1 - \beta_1^2)\omega}, \end{aligned} \tag{30}$$

$$\begin{aligned}\varphi_1' &= \frac{1}{2} - \frac{cK_p[(y_p - y_1 - \varepsilon_1\sin\varphi_1)\cos\varphi_1 - (x_p - x_1 - \varepsilon_1\cos\varphi_1)\sin\varphi_1]}{4\alpha_1\delta_1\varepsilon_1\omega} \\ &\quad - \frac{\beta_1^2 cK_p[(y_p - y_1 - \varepsilon_1\sin\varphi_1)\cos\varphi_1 - (x_p - x_1 - \varepsilon_1\cos\varphi_1)\sin\varphi_1]}{4\alpha_1\varepsilon_1\delta_1(\gamma_1\delta_1 - \beta_1^2)\omega} \\ &\quad + \frac{\beta_1^2 cK_p[(y_p - y_1 - \varepsilon_1\sin\varphi_1)\cos\varphi_1 + (x_p - x_1 - \varepsilon_1\cos\varphi_1)\sin\varphi_1]}{4\alpha_1\varepsilon_1\delta_1(\gamma_1\delta_1 - \beta_1^2)\omega}, \end{aligned} \tag{31}$$

$$\begin{aligned}\varepsilon_2' &= \frac{\beta_1 cK_p[(y_g - y_2 - \varepsilon_2\sin\varphi_2)\cos\varphi_2 - (x_g - x_2 - \varepsilon_2\cos\varphi_2)\sin\varphi_2]}{4\alpha_1(\gamma_1\delta_1 - \beta_1^2)\omega} \\ &\quad - \frac{\delta_1 cK_p[(x_g - x_2 - \varepsilon_2\cos\varphi_2)\cos\varphi_2 + (y_g - y_2 - \varepsilon_2\sin\varphi_2)\sin\varphi_2]}{4\alpha_1(\gamma_1\delta_1 - \beta_1^2)\omega}, \end{aligned} \tag{32}$$

$$\begin{aligned}\varphi_2' &= \frac{1}{2} - \frac{cK_p[(y_g - y_2 - \varepsilon_2\sin\varphi_2)\cos\varphi_2 - (x_g - x_2 - \varepsilon_2\cos\varphi_2)\sin\varphi_2]}{4\alpha_1\delta_1\varepsilon_2\omega} \\ &\quad + \frac{\beta_1^2 cK_p[(y_g - y_2 - \varepsilon_2\sin\varphi_2)\cos\varphi_2 + (x_g - x_2 - \varepsilon_2\cos\varphi_2)\sin\varphi_2]}{4\alpha_1\varepsilon_2\delta_1(\gamma_1\delta_1 - \beta_1^2)\omega} \\ &\quad - \frac{\beta_1\delta_1 cK_p[(x_g - x_2 - \varepsilon_2\cos\varphi_2)\cos\varphi_2 + (y_g - y_2 - \varepsilon_2\sin\varphi_2)\sin\varphi_2]}{4\alpha_1\varepsilon_2\delta_1(\gamma_1\delta_1 - \beta_1^2)\omega}, \end{aligned} \tag{33}$$

$$\begin{aligned}x_p'' &= -\frac{2\xi_2}{s}x_p' - \frac{1}{s^2}\left(x_p - x_1 - \varepsilon_1\cos\varphi_1\right) + \beta\cos(\phi/4) \\ &\quad - \frac{2\xi_3}{s}(x_p' - x_g' - E_p\sin\phi) - \frac{\Lambda}{s^2}(x_p - x_g - E_p\cos\phi), \end{aligned} \tag{34}$$

$$\begin{aligned}y_p'' &= -\frac{2\xi_2}{s}y_p' - \frac{1}{s^2}\left(y_p - y_1 - \varepsilon_1\sin\varphi_1\right) + \beta\sin(\phi/4) \\ &\quad - \frac{2\xi_3}{s}(y_p' - y_g' - E_p\cos\phi) - \frac{\Lambda}{s^2}(y_p - y_g - E_p\sin\phi) - \frac{f}{s^2}, \end{aligned} \tag{35}$$

$$\begin{aligned}x_g'' &= -\frac{2\xi_4}{s}x_g' - \frac{1}{s^2}\left(x_g - x_2 - \varepsilon_2\cos\varphi_2\right) + \beta_g\cos(\phi/8) \\ &\quad + \frac{2\xi_5}{s}(x_p' - x_g' - E_p\sin\phi) - \frac{\Lambda_g}{s^2}(x_p - x_g - E_p\cos\phi), \end{aligned} \tag{36}$$

$$\begin{aligned}y_g'' &= -\frac{2\xi_4}{s}y_g' - \frac{1}{s^2}\left(y_g - y_2 - \varepsilon_2\sin\varphi_2\right) + \beta_g\sin(\phi/8) \\ &\quad + \frac{2\xi_5}{s}(y_p' - y_g' - E_p\cos\phi) + \frac{\Lambda_g}{s^2}(y_p - y_g - E_p\sin\phi) - \frac{f_g}{s^2}, \end{aligned} \tag{37}$$

$$x_1'' + \frac{2\xi_1}{s_1}x_1' + \frac{1}{s_1^2}x_1 + \frac{\alpha_1}{s^2}x_1^3 - \frac{1}{2C_{1p}s^2}(x_p - x_1 - \varepsilon_1\cos\varphi_1) = 0, \tag{38}$$

$$y_1'' + \frac{2\xi_1}{s_1}y_1' + \frac{1}{s_1^2}y_1 + \frac{\alpha_1}{s^2}y_1^3 - \frac{1}{2C_{om}s^2}(y_p - y_1 - \varepsilon_1\sin\varphi_1) + \frac{f}{s^2} = 0, \tag{39}$$

$$x_2'' + \frac{2\xi_6}{s_2}x_2' + \frac{1}{s_2^2}x_2 + \frac{\alpha_2}{s^2}x_2^3 - \frac{1}{2C_{2p}s^2}(x_g - x_2 - \varepsilon_2\cos\varphi_2) = 0, \tag{40}$$

$$y_2'' + \frac{2\xi_6}{s_2}y_2' + \frac{1}{s_2^2}y_2 + \frac{\alpha_2}{s^2}y_2^3 - \frac{1}{2C_{2p}s^2}(y_g - y_2 - \varepsilon_2\sin\varphi_2) + \frac{f}{s^2} = 0, \tag{41}$$

where $\alpha_1 = -\frac{\mu L^3 R}{2c^2\psi}$, $\beta_1 = \int_0^\pi \sin\theta\cos\theta d\theta$, $\gamma_1 = \int_0^\pi \cos\theta\cos\theta d\theta$, $\delta_1 = \int_0^\pi \sin\theta\sin\theta d\theta$.

Eqs. (30)–(41) describe a non-linear dynamic system. In the current study, the approximate solutions of these coupled non-linear differential equations are obtained using the fourth order Runge–Kutta numerical scheme.

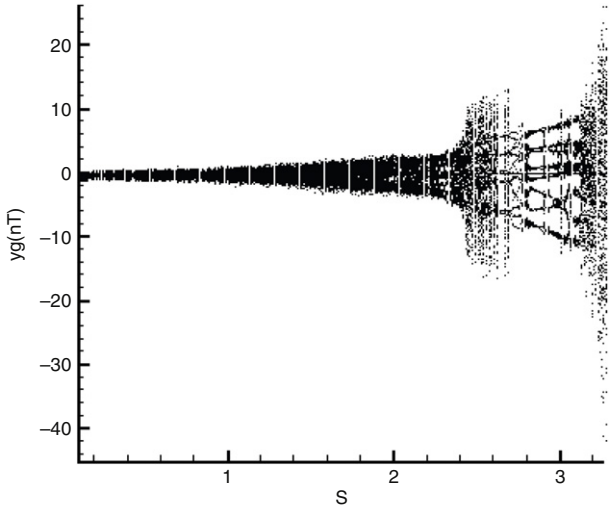

Fig. 3. Bifurcation diagrams of gear center using dimensionless rotational speed ratio, s, as bifurcation parameter ($\psi = 0.0$).

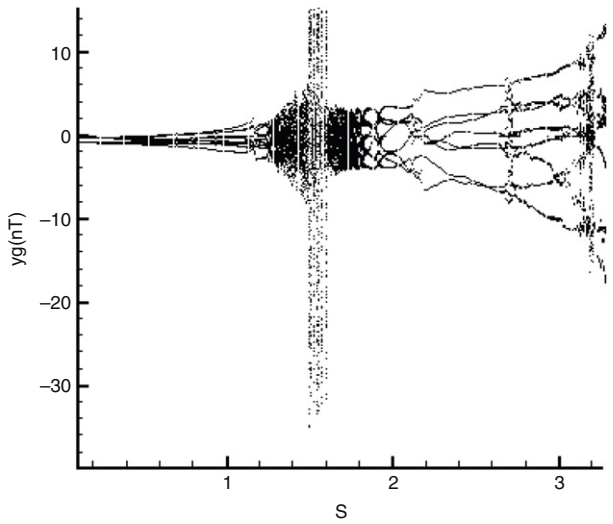

Fig. 4. Bifurcation diagrams of gear center using dimensionless rotational speed ratio, s, as bifurcation parameter ($\psi = 0.0001$).

3. Analytical tools for observing nonlinear dynamics of the gear-bearing system

In the present study, the nonlinear dynamics of the gear-bearing system shown in Fig. 1 are analyzed using Poincaré maps, bifurcation diagrams, the Lyapunov exponent and the fractal dimension. The basic principles of each analytical method are reviewed in the following sub-sections.

3.1. Dynamic trajectories and Poincaré maps

The dynamic trajectories of the gear-bearing system provide a basic indication as to whether the system behavior is periodic or non-periodic. However, they are unable to identify the onset of chaotic motion. Accordingly, some other form of analytical method is required. In the current study, the dynamics of the gear-bearing system are analyzed using Poincaré maps derived from the Poincaré section of the gear system. A Poincaré section is a hyper-surface in the state space transverse to the flow of the system of interest. In non-autonomous systems, points on the Poincaré section represent the return points of a time series corresponding to a constant interval T, where T is the driving period of the excitation force. The projection of the Poincaré section on the $y(nT)$ plane is referred to as the Poincaré map of the dynamic system. When the system performs

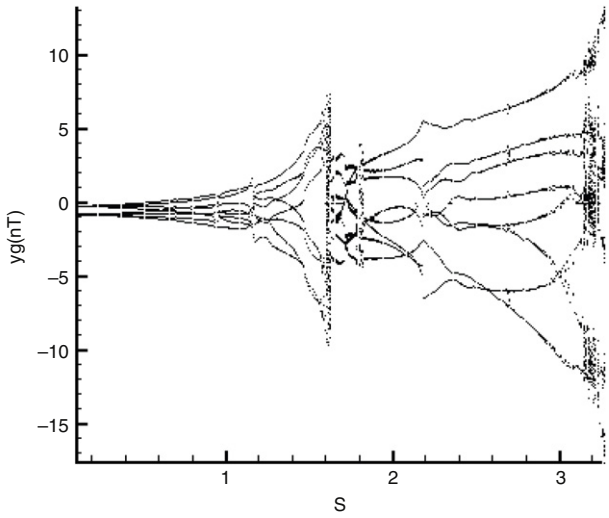

Fig. 5. Bifurcation diagrams of gear center using dimensionless rotational speed ratio, s, as bifurcation parameter ($\psi = 0.001$).

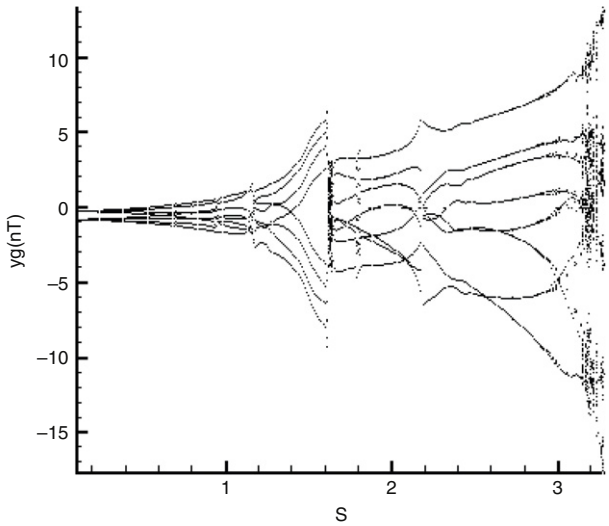

Fig. 6. Bifurcation diagrams of gear center using dimensionless rotational speed ratio, s, as bifurcation parameter ($\psi = 0.1$).

quasi-periodic motion, the return points in the Poincaré map form a closed curve. For chaotic motion, the return points form a fractal structure comprising many irregularly-distributed points. Finally, for nT-periodic motion, the return points have the form of n discrete points.

3.2. Power spectrum

In this study, the spectrum components of the motion performed by the gear-bearing system are analyzed by using the Fast Fourier Transformation method to derive the power spectrum of the displacement of the dimensionless dynamic transmission error. In the analysis, the frequency axis of the power spectrum plot is normalized using the rotational speed, ω.

3.3. Bifurcation diagram

A bifurcation diagram summarizes the essential dynamics of a gear-train system and is therefore a useful means of observing its nonlinear dynamic response. In the present analysis, the bifurcation diagrams are generated using two different

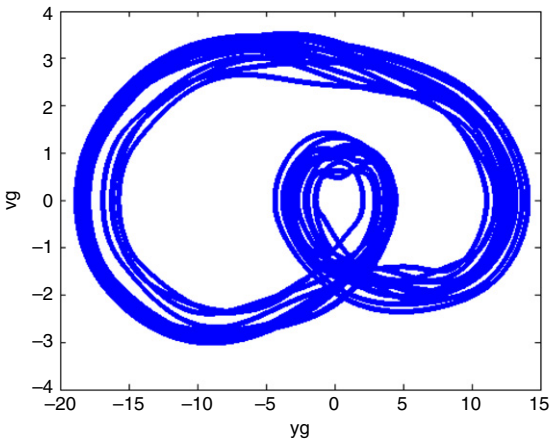

(a) Phase diagram.

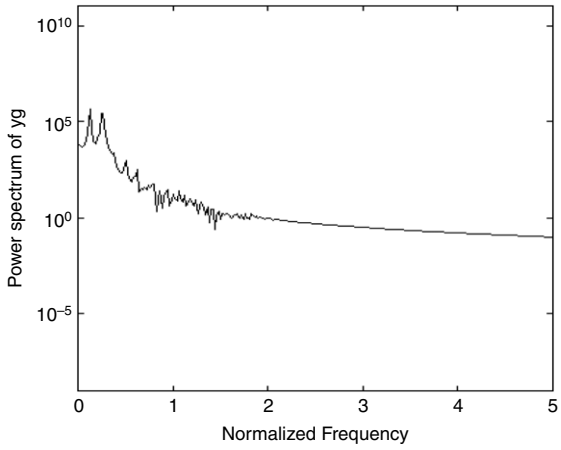

(b) Power spectrum.

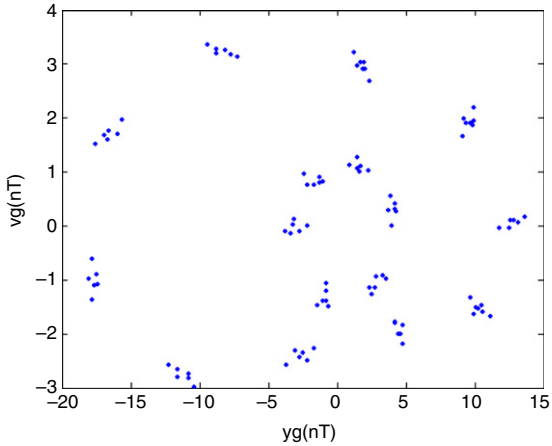

(c) Poincaré map.

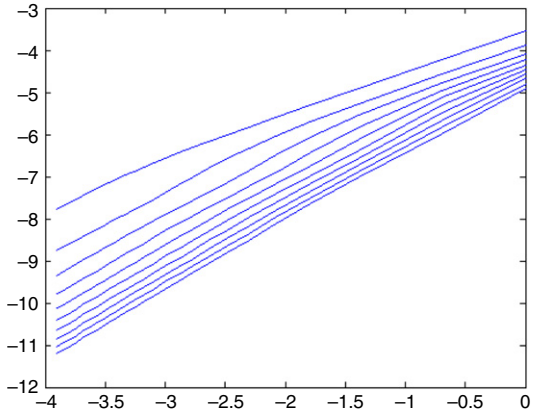

(d) Fractal dimension.

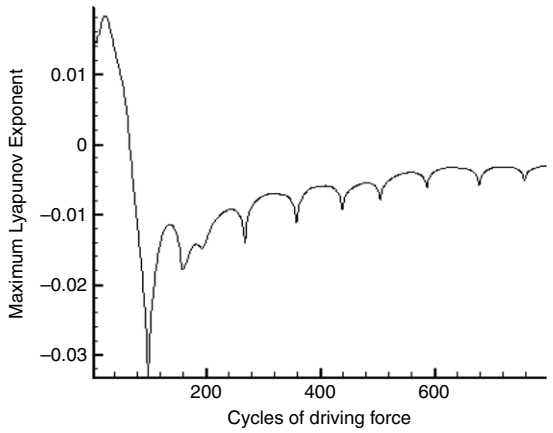

(e) Lyapunov exponent.

Fig. 7. Simulation results obtained for the gear-bearing system with $s = 3.27(y_g)$.

control parameters, namely the dimensionless unbalance coefficient, β, and the dimensionless rotational speed ratio, s, respectively. In each case, the bifurcation control parameter is varied with a constant step and the state variables at the end of one integration step are taken as the initial values for the next step. The corresponding variations of the $y(nT)$ coordinates of the return points in the Poincaré map are then plotted to form the bifurcation diagram.

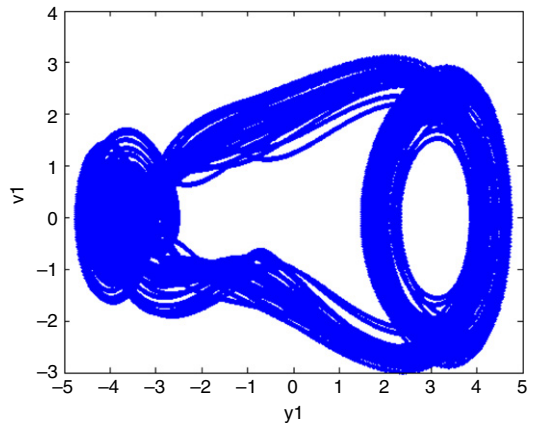

(a) Phase diagram.

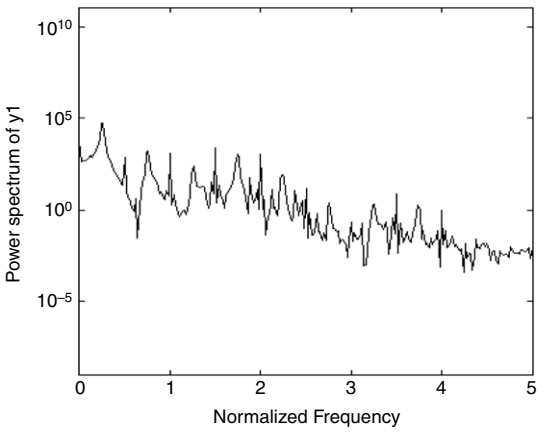

(b) Power spectrum.

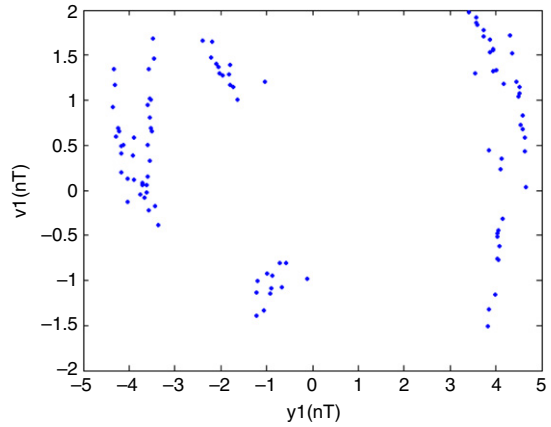

(c) Poincaré map.

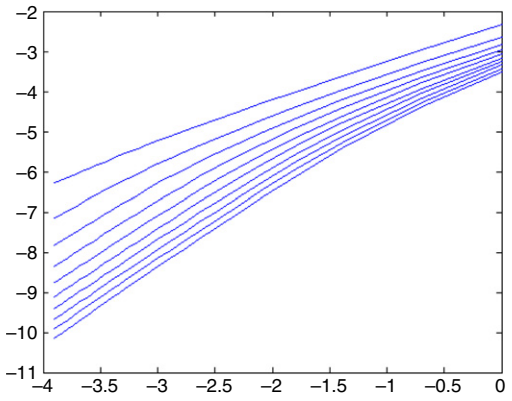

(d) Fractal dimension.

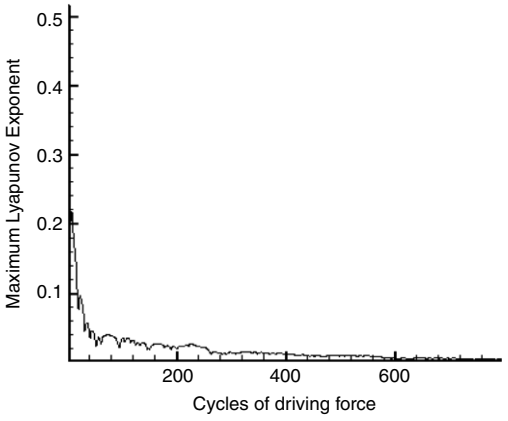

(e) Lyapunov exponent.

Fig. 8. Simulation results obtained for the gear-bearing system with $s = 3.27(y_1)$.

3.4. The Lyapunov exponent

The Lyapunov exponent of a dynamic system characterizes the rate of separation of infinitesimally close trajectories and provides a useful test for the presence of chaos. In a chaotic system, the points of nearby trajectories starting initially within a sphere of radius ε_0 form after time t an approximately ellipsoidal distribution with semi-axes of length $\varepsilon_j(t)$. The Lyapunov exponents of a dynamic system are defined by $\lambda_j = \lim_{t\to\infty} \frac{1}{t} \log \frac{\varepsilon_j(t)}{\varepsilon_0}$, where λ_j denotes the rate of divergence of the nearby

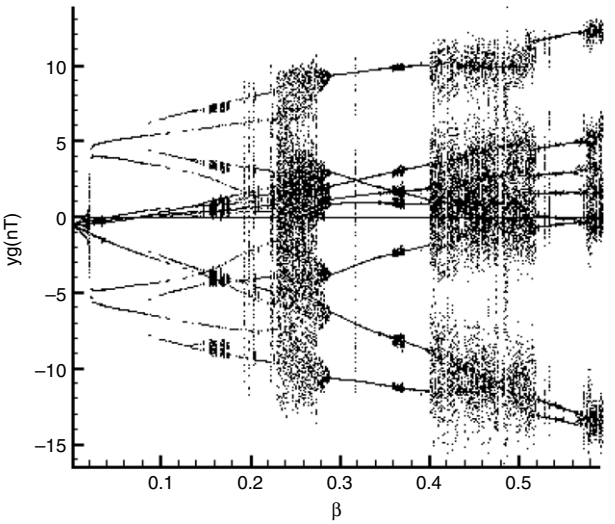

Fig. 9. Bifurcation diagrams of gear center using dimensionless unbalance parameter, β, as bifurcation parameter ($\psi = 0.1$).

trajectories. The exponents of a system are usually ordered into a Lyapunov spectrum, i.e. $\lambda_1 > \lambda_2 > \cdots > \lambda_m$. A positive value of the maximum Lyapunov exponent (λ_1) is generally taken as an indication of chaotic motion.

3.5. Fractal dimension

The presence of chaotic vibration in a system is generally detected using either the Lyapunov exponent or the fractal dimension property. The Lyapunov exponent test can be used for both dissipative systems and non-dissipative (i.e. conservative) systems, but is not easily applied to the analysis of experimental data. Conversely, the fractal dimension test can only be used for dissipative systems, but is easily applied to experimental data. In contrast to Fourier transform-based techniques and bifurcation diagrams, which provide only a general indication of the change from periodic motion to chaotic behavior, dimensional measures allow chaotic signals to be differentiated from random signals. Although many dimensional measures have been proposed, the most commonly applied measure is the correlation dimension *dG* defined by Grassberger and Proccacia due to its computational speed and the consistency of its results. However, before the correlation dimension of a dynamic system flow can be evaluated, it is first necessary to generate a time series of one of the system variables using a time-delayed pseudo-phase-plane method. Assume an original time series of $x_i = \{x(i\tau);\ i = 1, 2, 3, \ldots, N\}$, where τ is the time delay (or sampling time). If the system is acted upon by an excitation force with a frequency ω, the sampling time, τ, is generally chosen such that it is much smaller than the driving period. The delay coordinates are then used to construct an n-dimensional vector $X = (x(j\tau), x[(j+1)\tau], x[(j+2)\tau], \ldots, x[(j+n-1)\tau])$, where $j = 1, 2, 3, \ldots, (N - n + 1)$. The resulting vector comprises a total of $(N - n + 1)$ vectors, which are then plotted in an n-dimensional embedding space. Importantly, the system flow in the reconstructed n-dimensional phase space retains the dynamic characteristics of the system in the original phase space. In other words, if the system flow has the form of a closed orbit in the original phase plane, it also forms a closed path in the n-dimensional embedding space. Similarly, if the system exhibits a chaotic behavior in the original phase plane, its path in the embedding space will also be chaotic. The characteristics of the attractor in the n-dimensional embedding space are generally tested using the function $\sum_{i,j=1}^{N} H\left(r - |x_i - x_j|\right)$ to determine the number of pairs (i, j) lying within a distance $|x_i - x_j| < r$ in $\{x_i\}_{i=1}^{N}$, where H denotes the Heaviside step function, N represents the number of data points, and r is the radius of an n-dimensional hyper-sphere. For many attractors, this function exhibits a power law dependence on r as $r \to 0$, i.e. $c(r) \propto r^{d_G}$. Therefore, the correlation dimension, dG, can be determined from the slope of a plot of $[\log c(r)]$ versus $[\log r]$. Grassberger and Proccacia [25] showed that the correlation dimension represents the lower bound to the capacity or fractal dimension d_c, and approaches its value asymptotically when the attracting set is distributed more uniformly in the embedding phase space. A set of points in the embedding space is said to be fractal if its dimension has a finite non-integer value. Otherwise, the attractor is referred to as a 'strange attractor'. To establish the nature of the attractor, the embedding dimension is progressively increased, causing the slope of the characteristic curve to approach a steady state value. This value is then used to determine whether the system has a fractal structure or a strange attractor structure. If the dimension of the system flow is found to be fractal (i.e. to have a non-integer value), the system is judged to be chaotic.

In the current study, the attractors in the embedding space were constructed using a total of 60 000 data points taken from the time series corresponding to the displacement of the system. Via a process of trial and error, the optimum delay time when constructing the time series was found to correspond to one third of a revolution of the system. The reconstructed attractors were placed in embedding spaces with dimensions of $n = 2$, 4, 6, 8, 10, 12, 14, 16, 18, and 20, respectively,

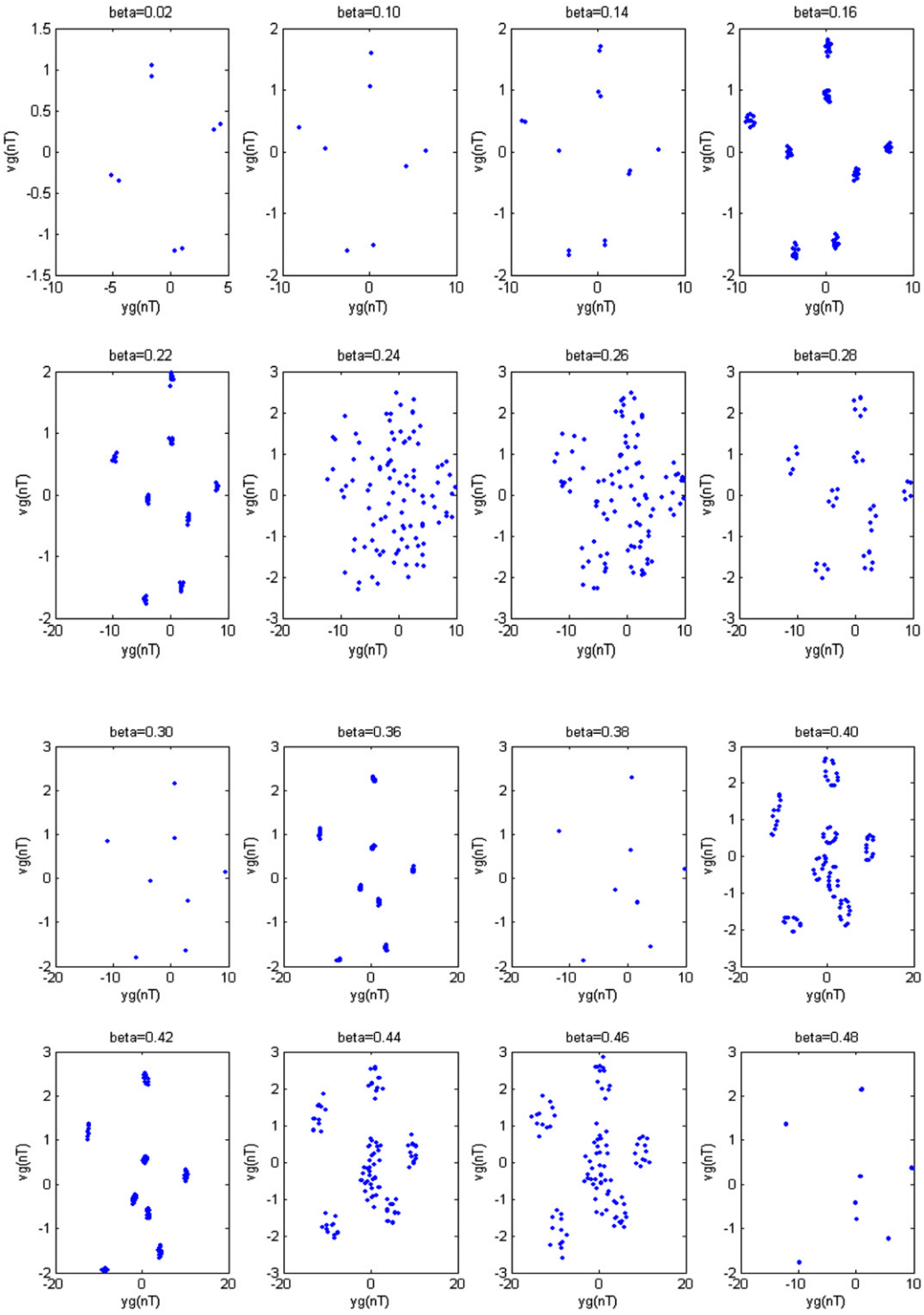

Fig. 10. Poincaré maps corresponding to different dimensionless unbalance parameters, β ($\psi = 0.1$).

yielding 10 different $[\log c(r)]$ versus $[\log r]$ plots for each attractor. The number of data points chosen for embedding purposes (i.e. 60 000) reflects the need for a compromise between the computation time and the accuracy of the results. In accordance with Chen and Yau [26], the number of points used to estimate the intrinsic dimension of the attracting set in

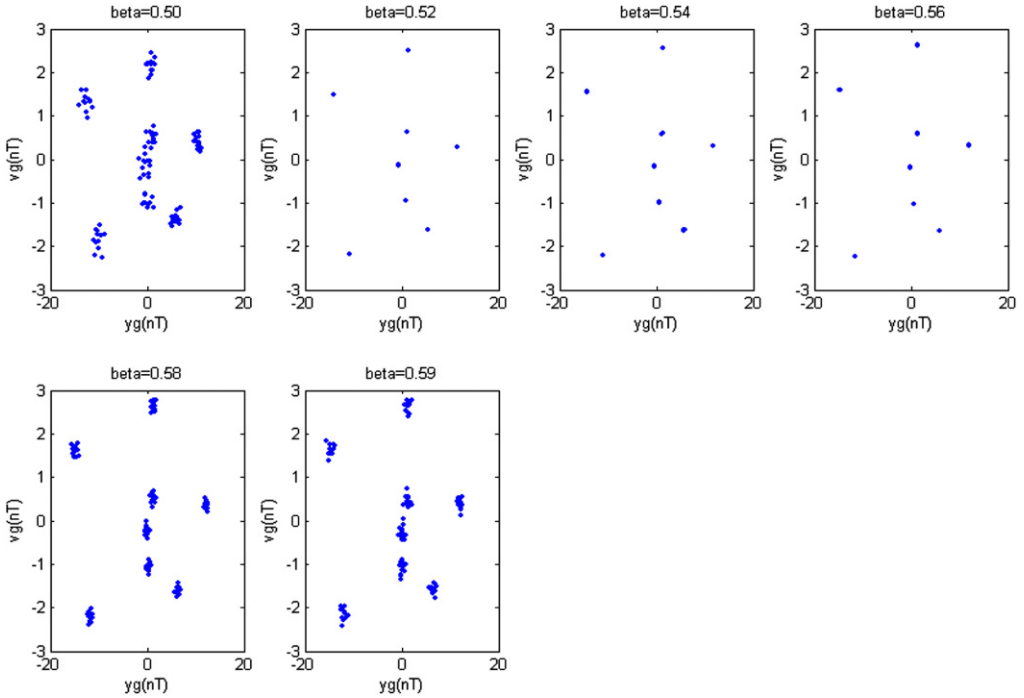

Fig. 10. (*continued*)

the current analysis is less than 42^M, where M is the greatest integer value less than the fractal dimension of the attracting set.

4. Numerical results and discussions

A number of parameters can be used to control the motion of the gear pair or bearing systems, e.g. the rotating speed, unbalance, damping coefficient, stiffness coefficient, etc. In practical bearing systems, the rotational speed ratio s is commonly used as a significant control parameter. Accordingly, the dynamic behavior of the current gear-bearing system was examined using the dimensionless rotational speed ratio s as a bifurcation control parameter. Fig. 3 presents the bifurcation characteristics of the gear center displacement in the vertical direction against the dimensionless rotational speed ratio, s with $\psi = 0.0$. It can be seen that at almost all rotating speeds the motion is non-periodic. We also can find that dynamic behaviors with $\psi = 0.0$ (zero permeability) are almost non-periodic and the dynamic amplitudes become greater and greater with increasing rotational speed ratios. In order to explorer different bifurcation phenomena and dynamic behaviors, other permeability is also taken into consideration. Fig. 4 shows the bifurcation diagram with $\psi = 0.0001$. The bifurcation diagram shows that at low rotating speeds the dynamic motion is sub-harmonic with period 8. At about $s > 1.18$ the motions becomes chaotic. The chaotic state remains for a short range of rotating speed ratios ($1.18 < s < 1.80$). At around $s = 1.48$–1.60, chaotic vibration also behaves highly amplitude and then the motion becomes $8T$ periodic motion at $s = 1.61$–3.10. Finally, at $s = 3.11$ it again becomes chaotic vibration. Fig. 5 is the bifurcation diagram with $\psi = 0.001$ and chaotic motions are found at $s = 1.60$–1.62 and $s > 3.15$. It performs sub-harmonic motions with period 8 at almost all another rotating speed ratios. With greater permeability for $\psi = 0.1$ as shown in Fig. 6 show that the vibration behaves $8T$ periodic motions for almost all the rotating speeds except at $s = 1.60$–1.62 and $s > 3.15$. We will not be able to distinguish dynamic behaviors to be chaotic or quasi-periodic motions only by dynamic orbits or bifurcation diagrams, but also use other schemes such as Poincaré maps, Lyapunov exponent or fractal dimension to specify our dynamic responses. Thus we introduce Figs. 7 and 8, i.e. phase diagram, power spectrum, Poincaré Map, Lyapunov exponent and fractal dimension for y_1 and y_g with $s = 3.27$, and we can find the simulation results are corresponding with one another. Phase diagrams show disordered dynamic behaviors; power spectra reveal numerous excitation frequencies; the return points in the Poincaré maps form geometrically fractal structures; the maximum Lyapunov exponent is positive; the fractal dimensions are found to be 1.39 for y_g and 1.43 for y_1.

The unbalance parameter is also an important control parameter for the vibration of gear, rotor and bearing systems. Therefore, we introduce the unbalance parameter as a control parameter to investigate vibration features. Fig. 9 is the bifurcation diagram of gear center using dimensionless unbalance parameter, β, as bifurcation control parameter. We also introduce Fig. 10 (Poincaré maps corresponding to different dimensionless unbalance parameters) to interpret dynamic behaviors more clearly. It can be seen that before $\beta = 0.16$ the dynamic motion performs nT-periodic and then it becomes chaotic and persist for a long period of time until $\beta > 0.28$. The dynamic motion returns to nT-periodic between

$0.28 < \beta < 0.40$. By $0.40 < \beta < 0.50$ make the motion become chaotic again, but it returns to nT-periodic as $\beta < 0.56$ afterward. Finally, the dynamic motion becomes chaotic when $\beta > 0.58$.

5. Conclusions

Effects of change in the rotating speed ratio and the unbalance parameter on the vibration features of the gear-bearing system are investigated theoretically in this paper. It can be seen that the system exhibits very rich forms of nT-periodic and chaotic vibrations. The bifurcation diagrams also reveal that greater values of permeability may not only improve non-periodic motions effectively, but also suppress dynamic amplitudes. Therefore, we may conclude that PSFD can improve dynamic stability of gear-bearing systems. Overall, the results presented in this study provide a detailed understanding of the nonlinear dynamic response of a gear-bearing system under typical unbalance approximations and rotational speed conditions. Specifically, the results enable suitable values of the unbalance coefficient and rotational speed ratio to be specified such that chaotic behavior can be avoided, thus reducing the amplitude of the vibration within the system and extending the system life.

References

[1] K. Ichimaru, F. Hirano, Dynamic behavior of heavy-loaded spur gears, Trans. ASME J. Eng. Ind. 22 (1974) 373–381.
[2] H.H. Lin, R.L. Huston, J.J. Coy, On dynamic loads in parallel shaft transmission: part 1—modeling and analysis, Trans. ASME J. Mech. Trans. Auto. Design 110 (1988) 221–225.
[3] A. Kahraman, R. Singh, Nonlinear dynamics of a spur gear pair, J. Sound Vib. 142 (1990) 49–75.
[4] K.Y. Yoon, S.S. Rao, Dynamic load analysis of spur gears using a new tooth profile, Trans. ASME J. Mech. Trans. Auto. Design 118 (1996) 1–6.
[5] M. Amabili, A. Fregolent, A method to identify model parameters and gear errors by vibrations of a spur gear pair, J. Sound Vib. 214 (2) (1998) 339–357.
[6] L. Vedmar, A. Anersson, A method to determine dynamic loads on spur gear teeth and on bearings, J. Sound Vib. 267 (2003) 1065–1084.
[7] H.N. Ozguven, D.R. Houser, Mathematical models used in gear dynamics, J. Sound Vib. 121 (1988) 383–411.
[8] H.N. Ozguven, D.R. Houser, Dynamic analysis of high speed gears by using loaded static transmission error, J. Sound Vib. 125 (1988) 71–83.
[9] Y. Cai, T. Hayashi, The linear approximated equation of vibration of a pair of spur gears, Trans. ASME J. Mech. Transm. Autom. Des. 116 (1994) 558–564.
[10] K. Umezawa, T. Sato, Simulation on rotational vibration of spur gears, Bull. Japan Soc. Mech. Eng. 27 (1984) 102–109.
[11] P.D. Mcfadden, M.M. Toozhy, Application of synchronous averaging to vibration monitoring of rolling element bearings, Mech. Syst. Signal Process. 14 (6) (2000) 891–906.
[12] L. Litvin, Q. Lian, A.L. Kapelevich, Asymmetric modified spur gear drives: reduction of noise, localization of contact, simulation of meshing and stress analysis, Comput. Methods Appl. Mech. Engrg. 188 (2000) 363–390.
[13] Y.H. Guan, M.F. Li, T.C. Lim, W.S. Shepard, Comparative analysis of actuator concepts for active gear pair vibration control, J. Sound Vib. 269 (2004) 273–294.
[14] D. Giagopulos, C. Salpistis, S. Natsiavas, Effect of non-linearities in the identification and fault detection of gear-pair systems, Internat. J. Non-Linear Mech. 41 (2006) 213–230.
[15] S. Theodossiades, S. Natsiavas, On geared rotordynamic systems with oil journal bearings, J. Sound Vib. 243 (4) (2001) 721–745.
[16] S. Theodossiades, S. Natsiavas, Periodic and chaotic dynamics of motor-driven gear-pair systems with backlash, Chaos Solitons Fractals 12 (2001) 2427–2440.
[17] C.W. Chang-Jian, C.K. Chen, Bifurcation and chaos of a flexible rotor supported by turbulent long journal bearings, Chaos Solitons Fractals 34 (2007) 1160–1179.
[18] C.W. Chang-Jian, C.K. Chen, Bifurcation analysis of flexible rotor supported by couple-stress fluid film bearings with non-linear suspension systems, Tribol. Int. 41 (2008) 367–386.
[19] C.C. Wang, C.Y. Lo, C.K. Chen, Nonlinear dynamic analysis of a flexible rotor supported by externally pressurized porous gas journal bearings, Trans. ASME J. Tribol. 124 (3) (2002) 553–561.
[20] C.C. Wang, C.K. Chen, Bifurcation analysis of externally pressurized porous gas journal bearings, Proc. Inst. Mech. Eng. Part C J. Mech. Eng. Sci. 217 (2003) 1325–1338.
[21] C.C. Wang, H.T. Yau, Application of the differential transformation method to bifurcation and chaotic analysis of an AFM probe tip, Comput. Math. Appl. 61 (8) (2011) 1957–1962.
[22] C.C. Wang, J.S. Wang, Analysis of herringbone-grooved gas journal-bearing system, J. Chin. Soc. Mech. Eng. 25 (2004) 189–197.
[23] C.W. Chang-Jian, H.T. Yau, HSFD-mounted rotor-bearing system lubricated with couple stress fluid with hydraulic control, J. Chin. Soc. Mech. Eng. 31 (4) (2010) 297–305.
[24] C.S. Liu, M.C. Tsai, R.H. Yen, P.D. Lin, C.Y. Chen, Design and experimental verification of novel hydrodynamic grooved journal bearing, J. Chin. Soc. Mech. Eng. 31 (2) (2010) 139–146.
[25] P. Grassberger, I. Proccacia, Characterization of strange attractors, Phys. Rev. Lett. 50 (1983) 346–349.
[26] C.L. Chen, H.T. Yau, Chaos in the imbalance response of a flexible rotor supported by oil film bearings with non-linear suspension, Nonlinear Dynam. 16 (1998) 71–90.